Synthesis of Silicates for High-Performance Oxide Semiconductors: Electronic Structure Analysis

Roberto C. Longo, Nils Schewe, Peter G. Weidler, Stefan Heissler, and Peter Thissen*

ABSTRACT: The demand for different materials in the field of semiconductors has been driving a strong research during the past decades. Few unique materials have been developed, and with additional modifications like crystal doping, it is now possible to achieve many of the desired material properties with atomic scale precision. An important roadblock for the scientific community lies in the fact that many of the materials being considered as channel replacements for silicon, like GaAs, indeed have well characterized and likely tunable electronic properties. On the other hand, such compounds are not suitable for mass production because they would represent both an increase in the demand of environmentally critical resources and safety concerns due to their toxic nature. In this work, we report the synthesis of three different silicates using a wet chemical approach, with a strict limitation to nontoxic and environmentally friendly resources. The atomic and electronic structure of the obtained oxides are characterized by X ray diffraction (XRD), infrared spectroscopy (IR), and diffuse reflection ultraviolet−visible spectroscopy (UV/vis) and subsequently examined by means of first principles calculations. Finally, we not only discuss possible limitations of the synthesized compounds but also anticipate further expansions of our approach to finally present the most likely fields of application.

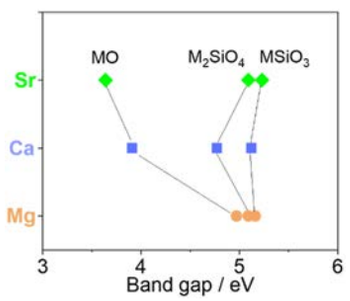

KEYWORDS: *silicates, alkaline earth metals, FT IR, XRD, UV/vis, density functional theory*

INTRODUCTION

The demand for new approaches in the information technology industry is increasingly fueled by the fundamental limitations arising from the constantly ongoing miniaturization of current semiconductor devices.[1] Novel concepts, such as the recently proposed quantum cellular automaton,[2] follow schemes complementary to pervasive current based architectures by exploiting the quantum nature at the molecular or atomic scale.

Recently, perovskites have attracted much attention in the research community due to their optoelectronic properties, low cost, and ease of the production process, besides their well known applications in photovoltaic (PV) devices.[3,4] Also, perovskite materials show several highlighted advantages in comparison to silicon based devices.[1] For instance, during the aging process of silicon, undesired effects such as depassivation of dangling bonds at grain boundaries or on the surface can develop, leading to electronic degradation.[5,6] In contrast, aging effects have proven to be less problematic for perovskite structures. Moreover, the use of several strategies such as ion substitution can further enhance their structural stability and usability spectrum.

From the environmental perspective, the production of crystalline, oxide free silicon can result in harmful health effects as well as present a negative environmental impact, which encourages the development and use of alternative materials such as perovskites.[7] However, it should also be noted that the presence of lead in most of the currently used perovskite materials can show damaging consequences for both the human organism and the environment.[3,8] In the recent years, this has led to the need of developing lead free perovskite materials.[9−11] An interesting alternative is given by the replacement of toxic lead by alkaline earth metals (Ca, Sr, Mg, and Ba) because of their similar ionic radii and charge states. Dismissing the toxic barium, the other three elements (magnesium, calcium, and strontium) represent a promising alternative, due to their nontoxicity and because they are between the 15 most abundant elements in the earth's crust.[12−14] When further substitution of titanium by silicon, environmentally friendly and nontoxic compounds can be acquired.

In this work we report on a novel wet chemical synthesis and the microscopic characterization of $MSiO_3$ type (M = Mg, Ca, Sr) materials as suitable alternatives for these new concepts of atomic scale information technology. The obtained crystalline silicate phases are proposed to be highly tunable and effective alternatives for common perovskites and III−V semiconductors. We will show the existing correlation between charge stability, charge transfer, electronic coupling, and chemical structure of the materials, also using first principles calculations to examine the atomic and electronic structure of the obtained compounds.

The different approaches employed in the synthesis and characterization of these materials will also be explained in detail.

The chemical stability of metal silicates against water is another important point. It depends principally on the metal to silicon ratio. Higher ratios (typically ~3) increase the reactivity toward water.[15,16] The best known example is the so called C_3S phases (tricalcium silicate, Ca_3SiO_5), produced in the cement industry, which are mixed with SiO_2 and water to form cement. The hydration of cement with water is composed of a series of chemical reactions that form the binding material. In other words, in the presence of water the calcium silicates hydration reaction products consist of a firm and hard calcium silicate hydrate mass.[17] The same chemical hydration concept can be applied to magnesium silicates (MS) and strontium silicates (SS), forming respectively magnesium silicate hydrates (MSH) and strontium silicate hydrates (SSH).

The other key aspect is the stability of the silicate phases against CO_2. CS phases tend to adsorb CO_2 and form carbonates. From this perspective, hydrated CS/CSH phases are promising candidates for CO_2 surface storage, but the overall impact of such a process on the mechanical properties of concrete remains unknown.[18] Interestingly, metal exchange in the silicates has shown a profound impact on the kinetics of carbonate formation. The formation of such carbonates on MS/MSH phases is kinetically hindered in comparison to the same reaction on CS/CSH phases.[19]

EXPERIMENTAL METHODS

Synthesis. All chemicals were used as received from Sigma Aldrich and VWR. The silicon single crystal disks were obtained from MicroChemicals GmbH. Samples have been prepared from silicon, water, and the corresponding alkaline earth metal hydroxides. Per sample, silicon (0.1000 g, 3.56×10^{-3} mol, 1 equiv) from a single crystal disk has been ground in an agate mortar to a particle size of about 30 μm. The powder was transferred to a centrifuge tube, and 5 mL of deionized water was added. Per sample, one of the alkaline earth metal hydroxides ($Mg(OH)_2$: 0.2289 g, 3.92×10^{-3} mol, 1.1 equiv; $Ca(OH)_2$: 0.2913 g, 3.93×10^{-3} mol, 1.1 equiv; $Sr(OH)_2$: 0.4774 g, 3.93×10^{-3} mol, 1.1 equiv) was added, and water was added to a total volume of 10 mL. The tubes were vigorously shaken and then opened and placed in a water bath at 60 °C for 48 h. During the reaction time they were shaken up every 12 h. The reaction mixtures were filtrated over cellulose filters; the sediments were air dried for 48 h. The resulting solids were finely ground in an agate mortar and then transferred into aluminum oxide crucibles. The crucibles were placed in an oven, where they were heated to 1100 °C with 2 °C/min, held at 1100 °C for 8 h, and then slowly cooled. The samples were transferred to plastic tubes and stored under nitrogen.

X-ray Diffraction (XRD). XRD measurements were performed on an Bruker D8 Advance instrument in Bragg–Brentano geometry (θ–θ setup) together with a PSD Lynxeye XE (192 Si strips) detector. The powders were finely ground in an agate mortar prior to measuring. Measurements were performed with a step size of 0.01° 2θ and a scan speed of 0.2 s/step (0.05° 2θ/s) in a range of $5° < 2\theta < 72°$ with Cu Kα (λ = 1.54186 Å) radiation. The diffractograms were evaluated with the Bruker DIFFRAC.EVA 5.2 software, the estimation of the quantitative composition, and determination of the mean coherence length (MCL, similar to crystallite sizes) were done via the Rietveld method (for details see ref 20) as implemented in the Bruker AXS TOPAS6.0 program.[21]

Fourier-Transform Infrared Spectroscopy. IR spectra measure ments were performed in transmission on a Bruker Alpha FT IR device. For the measurements, KBr pellets were prepared for each sample, containing 0.2000 g of KBr and 0.0030 g of the sample powder. A room temperature pyroelectric detector (DTGS) was employed for data collection. In a typical experiment, 512 scans were taken and averaged over three loops. Spectra were collected from 400 to 4000 cm^{-1} in transmission mode with a nominal resolution of 4 cm^{-1}.

UV/vis Spectroscopy. UV/vis spectra were measured on an Agilent instrument in diffuse reflection on quartz windows. Per sample a suspension of the powder in ethanol was prepared, applied on the window, and air dried. A barite doped PTFE window of the type Spectralon was used as reference.

Computational Details. First principles density functional theory (DFT) calculations were performed to determine the electronic structure and reaction enthalpies of the different compounds obtained. The simulations of the optimized geometries, relative energies, and orbital occupancies were performed by using DFT within the generalized gradient approximation, as implemented in Quantum Espresso.[22−24] The electron−ion interactions were described with ultrasoft pseudopotentials,[24] and the electronic wave functions were expanded into plane waves with a kinetic energy of 450 eV. The valence electron configurations used in our calculations are Mg ($2s^2p^63s^2$), Ca ($3s^2p^64s^2$), Sr ($4s^2p^65s^2$), Si ($3s^2p^2$), and O ($2s^2p^4$). The initial structures of all the compounds investigated were taken from the ICSD[25] and subsequently relaxed by using a conjugate gradient procedure, until the forces on the atoms were below 1 meV/Å. All the structural and geometrical details are provided in Table 4. The Brillouin zone integrations were done by using appropriate k meshes within the Monkhorst–Pack[26] scheme to ensure a convergence of 1 meV per supercell, and the PBE functional was used to describe the electron exchange and correlation energies within the generalized gradient approximation (GGA).[27]

RESULTS

The wet chemical synthesis method employed in this work is based on the well known industry process used in the production of calcium silicate phases, called the calcination of cement. In this process, mostly $CaCO_3$ and SiO_2 are milled, mixed, and kilned together.[28] Here we implement such a concept in the synthesis of other metal silicates, such as Mg and Sr silicates. The resulting powders are first analyzed by XRD to determine both the chemical composition of the obtained phases and their crystallinity.

For sample A (Figure 1A) three main phases have been found: silicon (Si, 29.0 ± 0.2 wt %), periclase (MgO, 39.9 ± 0.3 wt %), and forsterite (Mg_2SiO_4, 31.0 ± 0.2 wt %, orthorhombic system, space group *Pnma*). In contrast, larnite (Ca_2SiO_4, 54.7 ± 0.3 wt %, monoclinic system, space group $P2_1/n$) was the dominating phase in sample B (Figure 1B). Additional phases observed in this sample are lime (CaO, 18.1 ± 0.3 wt %) and silicon (Si, 27.2 ± 0.3 wt %). Finally, four phases were identified for sample C (Figure 1C), mainly Sr_2SiO_4 (86.0 ± 0.5 wt %, orthorhombic system, space group *Pmnbs*), followed by $SrSiO_3$ (11.6 ± 0.4 wt %, monoclinic system, space group *C*2/*c*), and traces of Sr_3SiO_5 (1.8 ± 0.1 wt %, tetragonal system, space group *P*4/*ncc*:2). The $SrSiO_3$ phase has not yet been provided with a name and was first referred to by Nishi et al. in 1997.[29] Some minor phases were also detected in this sample, mostly $SrSiO_3$ and Sr_3SiO_5. The calculated shares are presented in Table 1. According to this data, the samples did not contain quartz (SiO_2).

The size of the synthesized crystals (Table 2) is also relevant and can be determined from the integral of the corresponding X ray peaks. While a crystal size of 73 ± 2 nm was observed for the forsterite, larger sizes of 125 ± 15 and 140 ± 9 nm were obtained (via the Scherrer equation[30]) for larnite and $SrSiO_3$, respectively.

For instance, Zaid et al. were able to correlate the information about the crystal size and energy band gaps by electron scattering.[31] With the applied sintering method, the formation of tricalcium silicate phases was deliberately avoided. Tricalcium

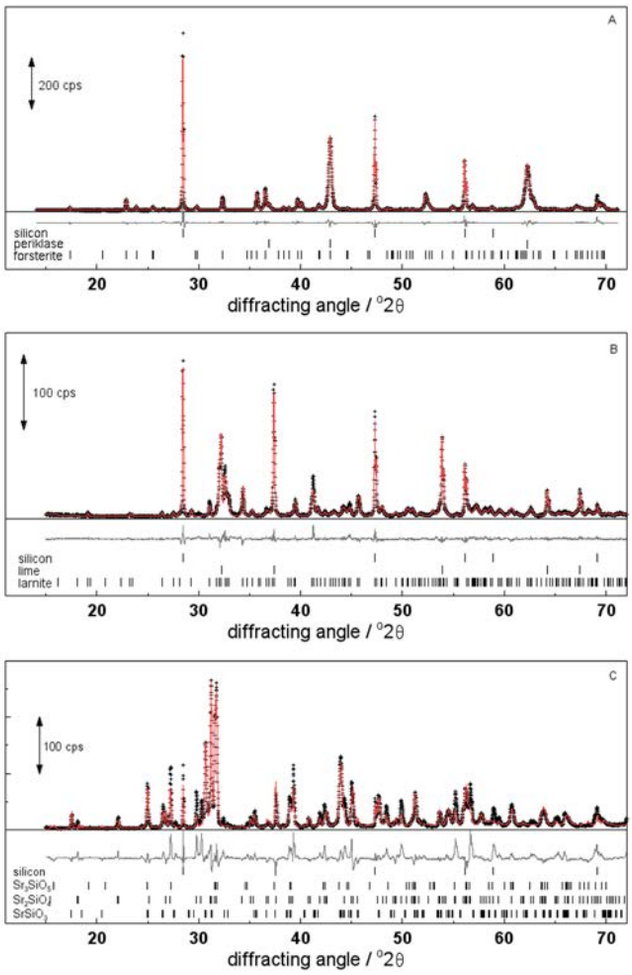

Figure 1. XRD patterns of the products of the three different reactions: (A) Si + $Mg(OH)_2$, (B) Si + $Ca(OH)_2$, and (C) Si + $Sr(OH)_2$. + represents the raw data, colored line the resultant fit, and gray line the difference curve (data − fit); the vertical bars mark the peak position of the respective mineral phase used in the fit.

silicate phases only form above 1400 °C and are metastable high temperature modifications.[32,33] It is to be noted that the crystal size can be influenced by the temperature, duration, and cooling profile of the heat treatment.[34] Because there is a correlation between the crystal size and the optical band gap,[35,36] the band gaps of all obtained materials can potentially be lowered further by adjusting the heat treatment process.

The IR data reflect the rather complicated nature of the samples. The spectra are shown in Figure 2 with the orange line corresponding to the magnesium sample, the blue line to the calcium sample, and the green line corresponding to the strontium sample. In the 1300−1550 cm^{-1} range, carbonate stretching modes can be observed in both the calcium and strontium containing samples, whereas they are absent in the magnesium sample. The occurrence of carbonate species in the optical spectra versus their absence in the crystallographic data is explained by them being located in amorphous phases. Also, they might be introduced by the brief handling of the samples in air while preparation of the KBr pellets. The silicate modes are roughly structured into two sets of bands. The higher frequency set between 935 and 1070 cm^{-1} shows a shift between samples, while the lower frequency set between 810 and 935 cm^{-1} shows constant band positions between samples with varying relative intensities. In the shifting band set, which is to be ascribed to silicate tetrahedral stretching with one nonbonding oxygen atom (NBO), the band maximum decreases with increasing mass of the alkaline earth metal. In detail, this mode ($\nu(Si{-}O^{-}{\sim}M^{2+})$) can be found at 1010 cm^{-1} in the spectrum measured from forsterite, 995 cm^{-1} for larnite, and 970 cm^{-1} for $SrSiO_3$. The absolute shifts are rather small, namely, 15 cm^{-1} between the magnesium and the calcium silicate peaks and 24 cm^{-1} between the calcium and the strontium silicate peaks. The overall trend can be understood via Hooke's law: when the metal atom is included in the reduced mass and we roughly assume a (O_3Si) group to be swinging against a (OM) group, the reduced masses increase with increasing mass of the metal, thus decreasing the frequency of the respective mode.

Both peak sets consist of multiple bands. This indicates a certain chemical heterogeneity in the silicate connections. Basically, all degrees of silicate condensation can be found throughout the respective samples. According to the literature, we ascribe the lower frequency set to the Si−O−Si asymmetric stretching mode ($\nu_{as}(Si{-}O{-}Si)$) at 900 cm^{-1} for all samples and the silicate tetrahedral stretching of silicate groups with two or three NBOs around that. The Si−O modes typically shift to lower energies with decreasing degree of interconnection. Because of the presence of multiple substances in each sample, an exact assignment of the bands and shoulders cannot be made.

Finally, we performed UV/vis spectroscopy to gain insight into the electronic structure of the materials. The collected spectra are shown in Figure 3. To determine the band gap, we transformed the UV/vis data into Tauc plots. The plot consists of $(\alpha h\nu)^2$ on the y axis and $h\nu$ (in eV) on the x axis. α is the absorption coefficient at a specific wavelength. This data is obtained by the transformation of the diffuse reflection R data via

$$\alpha(\lambda) = \frac{(1 - R(\lambda))^2}{2R(\lambda)} \quad (1)$$

From the obtained spectra one can determine the so called band edges of the synthesized silicate materials via Tauc transformation. The linear parts have undergone linear regression, resulting in band gap energies (x intercept of regression line). The results are presented in Table 3. In this case, direct band gaps have been assumed.

The feature in the low energy range of the magnesium compound spectrum, which has not been fitted, results in a band gap around 1.1 eV, clearly fitting that of silicon. This is in good

Table 1. Relative Amount of the Respective Substances in Each Sample (in wt %)[a]

	Si silicon	MgO periclase	Mg_2SiO_4 forsterite	CaO lime	Ca_2SiO_4 larnite	$SrSiO_3$	Sr_2SiO_4	Sr_3SiO_5
A	28.9 ± 0.2	39.2 ± 0.3	30.9 ± 0.2					
B	27.2 ± 0.3			18.1 ± 0.3	54.7 ± 0.3			
C	0.5 ± 0.1					11.6 ± 0.4	86.0 ± 0.5	1.8 ± 0.1

[a]Data are obtained from XRD measurements.

Table 2. Mean Crystallite Size of the Respective Substances in Each Sample (in nm)[a]

	Si silicon	MgO periclase	Mg_2SiO_4 forsterite	CaO lime	Ca_2SiO_4 larnite	$SrSiO_3$	Sr_2SiO_4	Sr_3SiO_5
A	420 ± 31	45 ± 3	73 ± 2					
B	183 ± 7			125 ± 17	125 ± 15			
C	179 ± 27					140 ± 9	116 ± 10	28 ± 6

[a]Data are obtained from XRD measurements.

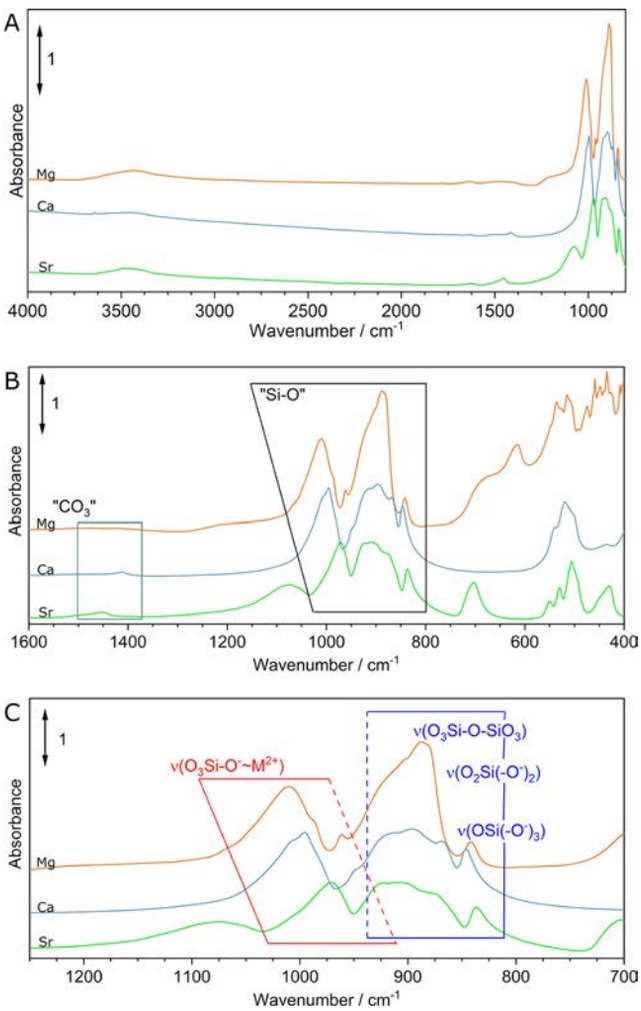

Figure 2. FT IR spectra of the magnesium (orange line), calcium (blue line), and strontium (green line) containing samples in the (A) full spectra, (B) fingerprint region, and (C) [Si−O] peak region. The red marked section encapsulates the shifting IR bands, and the blue marked section encapsulates the nonshifting IR bands.

accordance with the XRD measurements, which indicate a high amount of residual silicon in that sample. The visibility of silicon is mostly due to the mean crystallite size, which is around 420 nm in the magnesium sample, in comparison to around 180 nm in the other samples.

In view of the results, it becomes clear that a simple correlation between the band gap trends and the atomic mass of the metal is not possible, especially in view of the number of observed band gaps (two for magnesium compounds and four for both calcium and strontium compounds). As was stated previously, this points toward the presence of multiple phases in each sample. To further differentiate between the obtained band gaps and the species they arise from, it is necessary to resort to DFT calculations for a detailed characterization of the electronic structure.

To develop an overall picture of the coexistence of the different silicate phases as well as their atomic and electronic structure, DFT calculations were performed on a great variety of silicate compounds.

The main results are summarized in Table 4, but the basic idea can be described as follows. In any synthesis process, the use of wet chemical reactions makes impossible in practice to obtain single crystals or singular phases, therefore always ending up with phase mixtures or grain boundaries in crystals. However, heating the system allows to somehow control the thermodynamic ground state by driving the overall system to a certain phase of interest. From this perspective, one can consider the coexistence of the following silicate compounds and the corresponding decomposition reactions:

$$M_2SiO_4 \leftrightarrow MSiO_3 + MO \tag{2}$$

$$M_2SiO_4 \leftrightarrow 2MO + SiO_2 \tag{3}$$

$$2M_2SiO_4 \leftrightarrow MSiO_3 + 3MO + SiO_2 \quad (M = \text{Mg, Ca, or Sr}) \tag{4}$$

The change in the Gibbs free energy per compound unit, ΔG, can be used to study the driving factors leading to the predominance of M_2SiO_4 or the corresponding reaction products. Given the negligible entropy changes of the solid phases with temperature, ΔG can be expressed in a first approximation as

$$\Delta G = \Delta E_{\text{form}} \tag{5}$$

Therefore, in this work we use the Gibbs formation energies at both sides of reactions 2−4 to perform the thermodynamic analysis. Table 4 shows the total DFT energies per unit of compound as well as the change in the Gibbs free energy for the three decomposition reactions considered, which is given by

$$\Delta G = \Delta G_{\text{products}} - \Delta G_{\text{reactants}} \tag{6}$$

All the compounds listed in Table 4 have been studied following the crystal structures obtained in our experiments. For instance, forsterite and enstatite were chosen for Mg_2SiO_4 and $MgSiO_3$, whereas larnite and wollastonite were used for Ca_2SiO_4 and $CaSiO_3$. As mentioned previously, Sr including minerals have not yet been given an official name. Finally, standard cubic phases were used for MO compounds and the tetragonal crystalline phase for SiO_2.

The most noteworthy conclusion that can be inferred from the data shown in Table 4 is that there is a $\Delta E \sim 0.5$−0.6 eV difference between the formation energies per atom of $MSiO_3$ and M_2SiO_4 phases. On the contrary, the energy difference with respect to the cubic phases ranges from 2 eV (SrO and CaO) to 2.5 eV (MgO). Also, all the decomposition reactions listed in Table 4 display positive reaction energies; that is, M_2SiO_4 phases are thermodynamically favorable. Whereas the decomposition

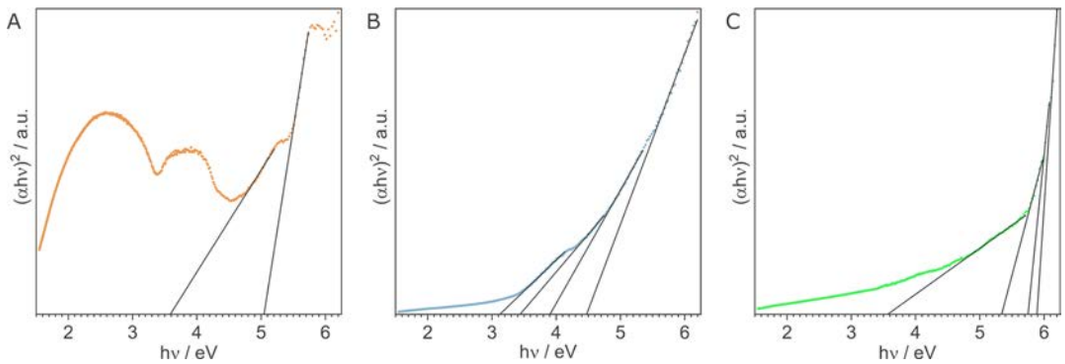

Figure 3. Tauc transformations of UV/vis spectra of the (A) magnesium (orange line) , (B) calcium (blue line) , and (C) strontium (green line) containing samples with linear fits (black lines).

Table 3. Electronic Properties Determined From UV/vis Spectra

incorporated metal	lowest band gap (eV)	highest band gap (eV)	observed band gaps (eV)	range (eV)
Mg	3.59	5.05	3.59	1.46
			5.05	
Ca	3.12	4.47	3.12	1.35
			3.44	
			3.90	
			4.47	
Sr	3.57	5.89	3.57	2.32
			5.34	
			5.75	
			5.89	

into MSiO$_3$ and the binary oxides MO seems plausible, although not spontaneous, the Gibbs reaction energies drastically increase if one includes SiO$_2$ in the picture. Therefore, in our experiments we probably obtained a mixture of the two scenarios. Furthermore, reaction energies increase with the atomic mass. Such growth might as well explain the better conversion efficiency observed for higher atomic numbers. Therefore, our results confirm that M_2SiO$_4$ silicate compounds are thermodynamically stable, not showing any tendency to decompose spontaneously into lower order silicates or binary oxides, in full agreement with the experimental evidence.

In a previous publication we obtained the disorder entropy of solid phases, which is of the order of a few to hundred units of the Boltzmann constant, depending on the stoichiometry.[37] Therefore, it would require, in units of $T\Delta S$, an extremely high temperature (of ∼1000−2000 K) in disorder entropy to overcome a difference of ∼0.5−1.0 eV in the Gibbs reaction energies. Phase transitions are then very unlikely once the silicate compounds have formed. Therefore, the results shown in Table 4 confirm the coexistence of the different silicate phases, as demonstrated by the XRD measurements. As described in the Experimental Methods, the sintering is carried out around 1373 K, which upon cooling does not leave enough residual heat for phase transformations driven by formation energy differences.

From a structural viewpoint, the M_2SiO$_4$ and MSiO$_3$ (M = Mg, Ca, and Sr) silicates listed in Table 4 display similar features, with some unique characteristics. Indeed, as can be seen in Figure 4, M_2SiO$_4$ geometries are formed by tilted MO$_6$ octahedra, connected or not by layers containing SiO$_4$ tetrahedra. Independently of the crystal group, Figure 4 shows that Mg$_2$SiO$_4$ contains layers without SiO$_4$ tetrahedra, whereas all Ca$_2$SiO$_4$ and Sr$_2$SiO$_4$ layers include SiO$_4$ units, although obviously each one of them connects two MO$_6$ octahedra due to the 2:1 M−Si stoichiometry. The structure of enstatite and wollastonite has been analyzed in detail in our previous publications,[38] but similarly to SrSiO$_3$, they all contain layers with SiO$_4$ connecting MO$_6$ octahedra. Finally, MO compounds show the standard, cubic MO$_6$ octahedral structure, with the octahedron axis aligned parallel to the out of plane direction. Table 4 also shows the range of M−O distances obtained in our calculations. As can be noted, d(Mg−O) < d(Ca−O) < d(Sr−O), as expected, whereas the Si−O tetrahedra display similar bond distances and therefore similar polyhedral volumes. The

Table 4. DFT Energy per Unit of Compound, Gibbs Reaction Energies per Unit of Compound (Eqs 2−4), Electronic Band Gap, Metal− and Silicon−Oxygen Distance, and Electronic Charge on the Metal Atom of the Silicate Structures Used in the Calculations; Information about SiO$_2$ Is Also Included for Completeness

compound	E_{form} (eV)	ΔG (eV) (eq 2)	ΔG (eV) (eq 3)	ΔG (eV) (eq 4)	gap (eV)	d(M O) (Å)	d(Si O) (Å)	Q(M) (e$^-$)
Mg$_2$SiO$_4$ (*Pnma*)	54.502	+0.247	+1.373	+0.720	5.09	2.07 2.23	1.61 1.66	8.33
Ca$_2$SiO$_4$ (*P*2$_1$/*c*)	57.043	+0.478	+1.094	+1.572	4.77	2.25 2.40	1.64	8.96, 9.04
Sr$_2$SiO$_4$ (*Pnma*)	60.767	+0.680	+1.654	+2.334	4.61	2.54 2.64	1.61 1.65	9.38, 9.53
MgSiO$_3$(*Pbca*)	42.425				5.16	2.03 2.18	1.57 1.67	8.30, 8.33
CaSiO$_3$ (*P*1)	43.775				5.12	2.37 2.63	1.59 1.67	8.89, 8.95
SrSiO$_3$ (*P*2$_1$/*c*)	45.715				5.23	2.42 2.75	1.58 1.69	9.44, 9.48
MgO (*Fm*3*m*)	11.830				4.97	2.12		8.50
CaO (*Fm*3*m*)	12.790				3.91	2.41		9.26
SrO (*Fm*3*m*)	14.372				3.64	2.60		9.55
SiO$_2$ (*I*42*d*)	30.369				6.28		1.60	

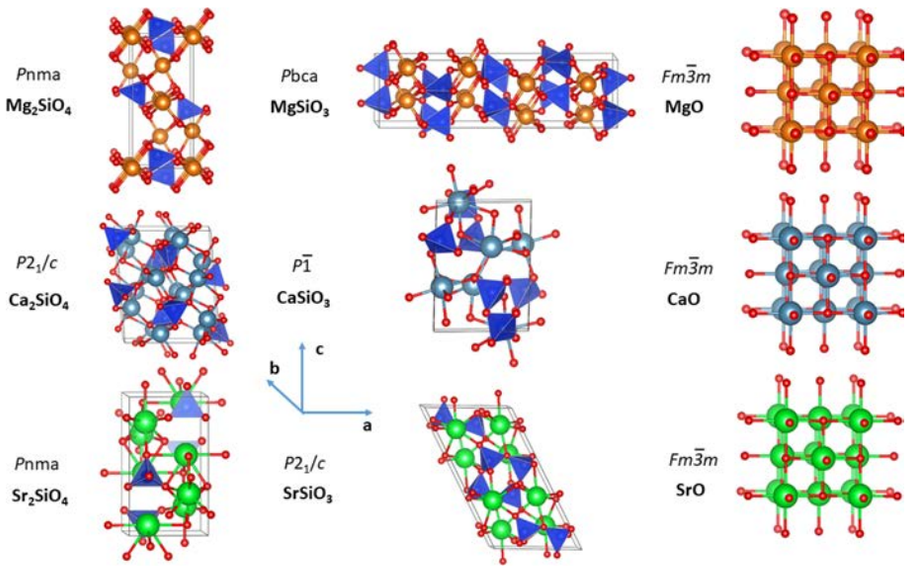

Figure 4. Calculated silicate and oxide structures with their respective space groups. Red and blue spheres represent oxygen and silicon atoms, respectively. The initial configurations were taken from the ICSD Web site.[25] The unit cells and axis vectors are also shown.

last column of Table 4 shows the electronic charge of metal *M* atoms. The initial valence electronic structure of the metal atoms included in the calculations was $ns^2np^6(n+1)s^2$. Although the charge around a specific atom always is a construct of the DFT calculations and *M* atoms are formally in a M^{2+} valence state, the results shown in Table 4 indicate that a larger atomic radius due to the increment of the quantum number of the outermost shell results in more charge located around the *M* atom, thus resulting in increased MO_6 octahedral volume, which ultimately leads to larger formation energies.

The electronic band structure displays similar features for each specific stoichiometry, irrespective of the metal atom of the silicate. Figure 5 shows the band structure of the relaxed supercells of Mg , Ca , and Sr containing compounds. Given their similarities, we will only discuss here the features of Sr containing compounds, which have not been reported previously. As can be seen in the figure, Sr_2SiO_4 has a direct band gap, located at the Γ point. The valence band states show large dispersion, less pronounced in the conduction band minimum (CBM). On the contrary, $P2_1/c$ $SrSiO_3$ shows an indirect band gap, with the valence band maximum (VBM) at the C high symmetry point and the CBM at the Γ point, although the extremely large dispersion of the valence states makes the location of the VBM hardly relevant. Finally, the SrO band diagram shows the standard features of cubic compounds, with a Γ−X indirect band gap and relatively low dispersion (thus higher electron velocity and electronic conductivity), especially along the K−Γ and Γ−L high symmetry lines.

The band gaps obtained in our experiments show a large range of values. For instance, the largest value found for Mg compounds (5.05 eV) agrees relatively well with our calculations (5.09−5.16 eV), but the lowest value (3.59 eV) is considerably smaller, thus suggesting the possibility of the presence of magnesium silicates ($MgO{\cdot}xSiO_2$). On the contrary, the band gaps of Ca compounds (3.12−4.47 eV) and Sr compounds (3.57−5.89 eV) agree relatively well with those obtained in our calculations, as can be seen in Table 4. Although it is well known that PBE DFT tends to underestimate the electronic band gaps, it is also certain that such difference is much lower for ternary silicate compounds of the form M_2SiO_4 or $MSiO_3$[39] than for pure ionic compounds, where the difference can reach up to 2.8 eV for MgO.[40] However, the specific values affect neither the observed trends nor the main conclusions of this work. Altogether, it has been demonstrated that the range of band gaps obtained in the UV/vis spectra can be accurately identified with a specific geometry by means of DFT calculations.

DISCUSSION

The absence of SiO_2 in the diffraction data indicates that the aforementioned transformation of the different phases occurs in such a way that the cohesion energy is increased. During the sintering step at the end of the experimental routine, all the quartz that might have been formed during the wet chemical steps was effectively transformed into the respective M_2SiO_4 or $MSiO_3$ stoichiometries. This process also consumed parts of the residual metal oxides and hydroxides.

The unreacted silicon content of the samples, as outlined by the XRD and UV/vis measurements, is the highest in the magnesium sample, the lowest in the calcium compounds, and almost nonexistent in the strontium sample. This correlates well with the solubility and the basicity of the respective metal hydroxides in water.[41] Furthermore, this correlates with the received particle size, which increases with increasing reactivity of the metal hydroxide. As was outlined, this in turn directly influences the obtained band gaps, such that especially for the magnesium samples the observed values are expected to be substantially larger than for the respective bulk material. The presented wet chemical synthesis thus seems to be most applicable for the highly alkaline strontium compounds.

The IR data show shifting and nonshifting silicate band sets. The shift between the samples is smaller than expected within Hooke's law.[42] The average chain length of alkaline earth metal silicates was previously shown to have an impact on the Si−O band position.[43] Because this degree of condensation scales with the M/Si ratio of the silicate phases, which again should be different between samples due to the reactivity of the respective metals, different mean chain lengths are expected. Based on the almost constant band positions in the nonshifting set, this explanation is ruled out, since it should affect all Si−O bands.

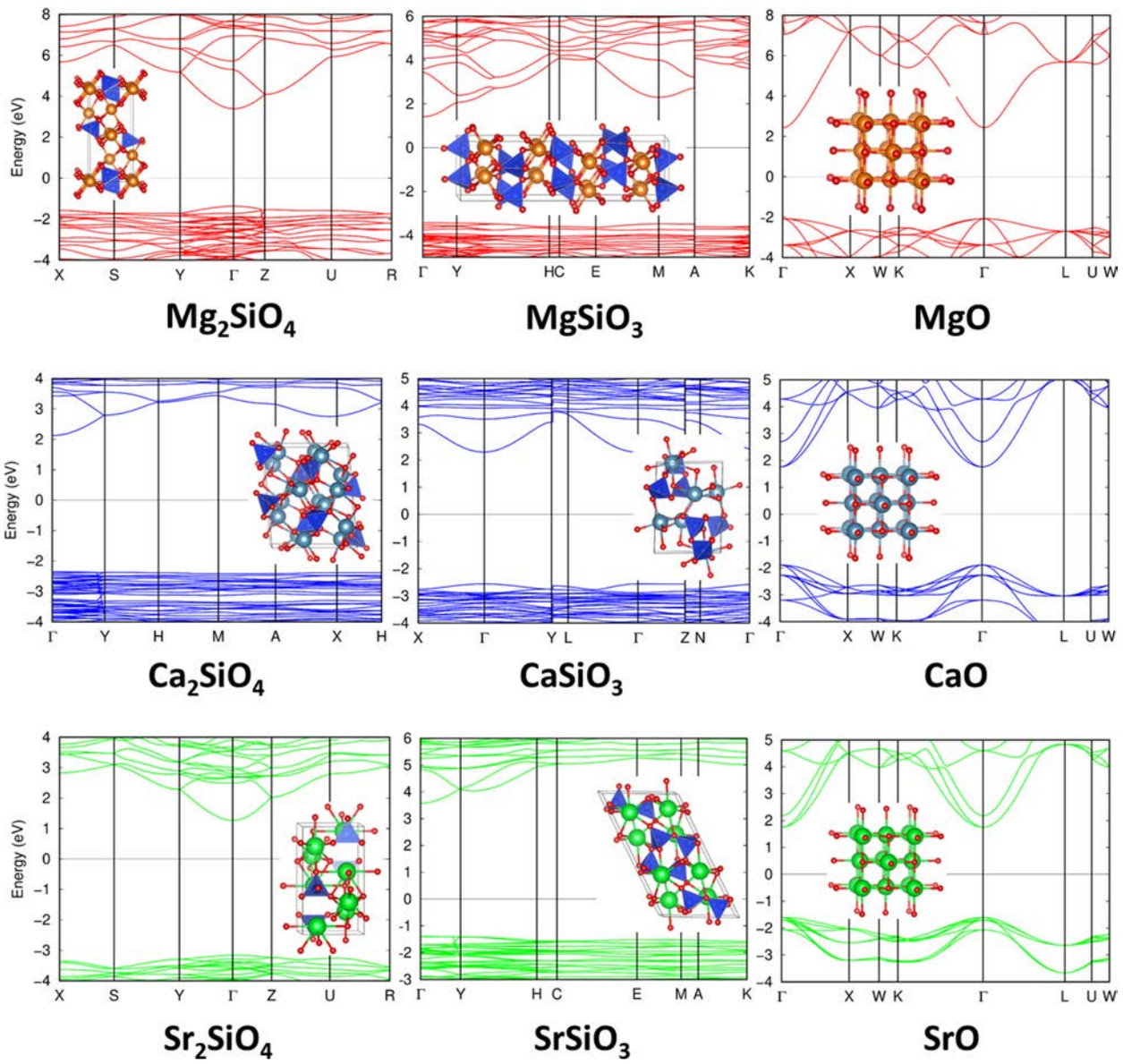

Figure 5. Electronic band structure of Mg , Ca , and Sr containing compounds.

Notably, Hooke's law does not fully apply in the present case. The force constant of the observed mode (i.e., Si−O stretching) is altered by the neighboring charge density distribution while there also is a change in the reduced mass of the vibrating components. In some cases, the description of the two sets of silicate bands as optical phonons is very popular. Given the crystallinity of the samples, the higher energy (shifting) IR band set may be described as longitudinal optical phonon (LO) and the lower energy (nonshifting) IR band set as transversal optical phonon (TO).[44,45] The fact that they do not shift together, as is often observed in samples with varying grain sizes and degree of condensation of the silicate, makes it very plausible that the alkaline earth metals mass is mostly responsible for the band shift. As mentioned before, the high number of observed bands and the heterogeneity of the samples inhibit full band assignment.

The differentiation between shifting and nonshifting bands is understandable in this context, given that the frequency of a silicate group with only one NBO can effectively be altered by the positive charge of a metal cation coordinating that free oxygen atom. Therefore, the metal specific influence on the band position is rather large, giving rise to a shifting band set. The influence of the metal atom on the silicate with more NBOs is also due to symmetry, smaller, resulting in almost negligible relative shifts of the corresponding IR peaks and a nonshifting band set.

Although the Goldschmidt rule for perovskite stability is fulfilled for the discussed stoichiometries,[46] no perovskite phases are found in the samples. Notably, and according to the literature, this fulfillment does not automatically imply the formation of perovskites. This matches our findings regarding the respective formation energies shown.

As has been discussed previously, the perovskite modifica tions of the present silicates are only stable at dramatically high pressures. Upon decompression, most of these phases undergo amorphization, leading to substances without desirable proper ties. The presented methodology includes sintering as the last step, which has three critical effects: the removal of carbon

compounds, the conversion of quartz and unreacted components toward the desired silicates, and recrystallization of the latter.

The XRD measurements show the crystalline nature of the prepared samples. This is in contrast to CSH phases typically obtained in wet chemical synthesis and in line with the perovskite structures opted to be substituted in the future. The UV/vis spectra and the DFT calculations of the electronic structures of the synthesized compounds show a relatively good agreement, thus outlining their potential for commercial use as semiconductors.

The silicate compounds presented in this work must be evaluated for both their crystallographic stability (i.e., stability against decomposition, irrespective of environmental conditions) and their chemical stability under environmental conditions. However, the long term chemical stability of calcium containing silicates in water and carbon dioxide rich environments is presumably low.[17] But such hypothetical instability can be seen as an opportunity: when aiming for semiconductor materials with specific band gaps, the so called metal−proton and metal−metal exchange reactions (MPER and MMER[17,19]) offer an accessibility to highly tunable band gaps, even after the synthesis of the corresponding compound. However, higher level processes like monolayer doping[47] have yet to be implemented for the compounds presented in this work.

Last, tunable silicate based semiconductors are composed of low price materials; they are easy to synthesize and environmentally friendly due to the broad availability of the base materials. Moreover, unlike III−V compounds such as gallium arsenide and lead based perovskites, they do not pose any health concern and can thus be used in a wider variety of applications. Our synthesis and characterization of these materials provide enough insights for any device building application in the field of semiconductor oxides. The synthesis process can easily be transferred to silicon wafers.[48] From there, selective sensors for infrared and other spectroscopy techniques can be created. Furthermore, because of the high temperature robustness, the thin films can be used to dope silicon wafers and produce, for example, solar cells. In contrast to other modern technologies, like monolayer doping (MLD),[37] the doping based on metal silicate films is not limited to one monolayer. Another outstanding point of the metal silicate films is that they can be etched from the carrying silicon wafer without HF, in contrast to silicon oxide.[49] In the synthesis different metal sources can be integrated and even combined. For the community of light emitting sources and the photocatalytic field this opens chemically easy ways to dope the structures with rare metals.[50,51]

CONCLUSIONS

In this work we have demonstrated an extremely sustainable approach to synthesize silicate compounds based on three different metals, namely magnesium, calcium, and strontium. Structural analysis performed by XRD confirms the success of the synthesis, additionally solving previous discrepancies in crystal sizes based on the reacted chemical compounds. FT IR spectroscopy was able to further underline the presence of the three different metals in the synthesized silicates as the driving trend for the shifted Si−O−M peaks. By means of UV/vis spectroscopy, the electronic band gaps were obtained, which show multiple band gaps for every sample. The obtained trend agrees well with the results of DFT calculations, and the wide range of band gaps obtained in the experiments can be attributed to specific compounds following atomic scale simulations.

Our approach has additional potentialities, for instance, by introducing a possible wet chemical reaction to decorate the synthesized material with other metals. Combining the synthesis process described in this work with high level processes such as monolayer doping would lead to sustainable, tunable, and environmentally friendly semiconductor materials to be used in novel electronic devices.

AUTHOR INFORMATION

Corresponding Author

Peter Thissen − *Institut für Funktionelle Grenzflächen (IFG), Karlsruher Institut für Technologie (KIT), 76344 Eggenstein Leopoldshafen, Germany;* orcid.org/0000 0001 7072 4109; Email: peter.thissen@kit.edu

Authors

Roberto C. Longo − *Tokyo Electron America, Inc., Austin, Texas 78741, United States;* orcid.org/0000 0003 4353 841X

Nils Schewe − *Institut für Funktionelle Grenzflächen (IFG), Karlsruher Institut für Technologie (KIT), 76344 Eggenstein Leopoldshafen, Germany;* orcid.org/0000 0001 6283 4834

Peter G. Weidler − *Institut für Funktionelle Grenzflächen (IFG), Karlsruher Institut für Technologie (KIT), 76344 Eggenstein Leopoldshafen, Germany*

Stefan Heissler − *Institut für Funktionelle Grenzflächen (IFG), Karlsruher Institut für Technologie (KIT), 76344 Eggenstein Leopoldshafen, Germany*

Notes

The authors declare no competing financial interest.

ACKNOWLEDGMENTS

P.T. acknowledges the DFG for financial support.

REFERENCES

(1) Snaith, H. J. Present status and future prospects of perovskite photovoltaics. *Nat. Mater.* **2018**, *17* (5), 372−376.

(2) Sarvaghad Moghaddam, M.; Orouji, A. A. New symmetric and planar designs of reversible full adders/subtractors in quantum dot cellular automata. *Eur. Phys. J. D* **2019**, *73* (6), 125.

(3) Wu, M. C.; Chen, W. C.; Chan, S. H.; Su, W. F. The effect of strontium and barium doping on perovskite structured energy materials for photovoltaic applications. *Appl. Surf. Sci.* **2018**, *429*, 9−15.

(4) Kojima, A.; Teshima, K.; Shirai, Y.; Miyasaka, T. Organometal Halide Perovskites as Visible Light Sensitizers for Photovoltaic Cells. *J. Am. Chem. Soc.* **2009**, *131* (17), 6050.

(5) Steirer, K. X.; Schulz, P.; Teeter, G.; Stevanovic, V.; Yang, M.; Zhu, K.; Berry, J. J. Defect Tolerance in Methylammonium Lead Triiodide Perovskite. *ACS Energy Letters* **2016**, *1* (2), 360−366.

(6) Kim, J.; Lee, S. H.; Lee, J. H.; Hong, K. H. The Role of Intrinsic Defects in Methylammonium Lead Iodide Perovskite. *J. Phys. Chem. Lett.* **2014**, *5* (8), 1312−1317.
(7) Celik, I.; Phillips, A. B.; Song, Z. N.; Yan, Y. F.; Ellingson, R. J.; Heben, M. J.; Apul, D. Environmental analysis of perovskites and other relevant solar cell technologies in a tandem configuration. *Energy Environ. Sci.* **2017**, *10* (9), 1874−1884.
(8) Gracia, R. C.; Snodgrass, W. R. Lead toxicity and chelation therapy. *Am. J. Health Syst. Pharm.* **2007**, *64* (1), 45−53.
(9) Kulkarni, A.; Singh, T.; Ikegami, M.; Miyasaka, T. Photovoltaic enhancement of bismuth halide hybrid perovskite by N methyl pyrrolidone assisted morphology conversion. *RSC Adv.* **2017**, *7* (16), 9456−9460.
(10) Park, B. W.; Philippe, B.; Zhang, X. L.; Rensmo, H.; Boschloo, G.; Johansson, E. M. J. Bismuth Based Hybrid Perovskites $A_3Bi_2I_9$ (A: Methylammonium or Cesium) for Solar Cell Application. *Adv. Mater.* **2015**, *27* (43), 6806.
(11) Singh, T.; Kulkarni, A.; Ikegami, M.; Miyasaka, T. Effect of Electron Transporting Layer on Bismuth Based Lead Free Perovskite $(CH_3NH_3)_3$ Bi_2I_9 for Photovoltaic Applications. *ACS Appl. Mater. Interfaces* **2016**, *8* (23), 14542−14547.
(12) Jacobsson, T. J.; Pazoki, M.; Hagfeldt, A.; Edvinsson, T. Goldschmidt's Rules and Strontium Replacement in Lead Halogen Perovskite Solar Cells: Theory and Preliminary Experiments on $CH_3NH_3SrI_3$. *J. Phys. Chem. C* **2015**, *119* (46), 25673−25683.
(13) Pazoki, M.; Jacobsson, T. J.; Hagfeldt, A.; Boschloo, G.; Edvinsson, T. Effect of metal cation replacement on the electronic structure of metalorganic halide perovskites: Replacement of lead with alkaline earth metals. *Phys. Rev. B: Condens. Matter Mater. Phys.* **2016**, *93* (14), 144105.
(14) Uribe, J. I.; Ramirez, D.; Osorio Guillen, J. M.; Osorio, J.; Jaramillo, F. $CH_3NH_3CaI_3$ Perovskite: Synthesis, Characterization, and First Principles Studies. *J. Phys. Chem. C* **2016**, *120* (30), 16393−16398.
(15) Izadifar, M.; Königer, F.; Gerdes, A.; Wöll, C.; Thissen, P. Correlation between Composition and Mechanical Properties of Calcium Silicate Hydrates Identified by Infrared Spectroscopy and Density Functional Theory. *J. Phys. Chem. C* **2019**, *123* (17), 10868−10873.
(16) Giraudo, N.; Weidler, P. G.; Laye, F.; Schwotzer, M.; Lahann, J.; Wöll, C.; Thissen, P. Corrosion of Concrete by Water Induced Metal Proton Exchange. *J. Phys. Chem. C* **2016**, *120* (39), 22455−22459.
(17) Thissen, P.; Natzeck, C.; Giraudo, N.; Weidler, P.; Wöll, C. Hydration of Concrete: The First Steps. *Chem. Eur. J.* **2018**, *24* (34), 8603−8608.
(18) Giraudo, N.; Thissen, P. Carbonation Competing Functionaliza tion on Calcium Silicate Hydrates: Investigation of Four Promising Surface Activation Techniques. *ACS Sustainable Chem. Eng.* **2016**, *4* (7), 3985−3994.
(19) Longo, R. C.; Königer, F.; Nefedov, A.; Thissen, P. Chemical Properties of Metal Silicates Rendered by Metal Exchange Reaction. *ACS Sustainable Chem. Eng.* **2019**, *7* (9), 8449−8457.
(20) Young, R. A. *The Rietveld Method*; International Union of Crystallography: 1995; p 308.
(21) Thissen, P.; Cho, K.; Longo, R. C. Nanopatterning of Group V Elements for Tailoring the Electronic Properties of Semiconductors by Monolayer Doping. *ACS Appl. Mater. Interfaces* **2017**, *9* (2), 1922−1928.
(22) Giannozzi, P.; Andreussi, O.; Brumme, T.; Bunau, O.; Buongiorno Nardelli, M.; Calandra, M.; Car, R.; Cavazzoni, C.; Ceresoli, D.; Cococcioni, M.; Colonna, N.; Carnimeo, I.; Dal Corso, A.; de Gironcoli, S.; Delugas, P.; DiStasio, R. A.; Ferretti, A.; Floris, A.; Fratesi, G.; Fugallo, G.; Gebauer, R.; Gerstmann, U.; Giustino, F.; Gorni, T.; Jia, J.; Kawamura, M.; Ko, H. Y.; Kokalj, A.; Küçükbenli, E.; Lazzeri, M.; Marsili, M.; Marzari, N.; Mauri, F.; Nguyen, N. L.; Nguyen, H. V.; Otero De La Roza, A.; Paulatto, L.; Poncé, S.; Rocca, D.; Sabatini, R.; Santra, B.; Schlipf, M.; Seitsonen, A. P.; Smogunov, A.; Timrov, I.; Thonhauser, T.; Umari, P.; Vast, N.; Wu, X.; Baroni, S. Advanced capabilities for materials modelling with Quantum ESPRESSO. *J. Phys.: Condens. Matter* **2017**, *29* (46), 465901.
(23) Giannozzi, P.; Baroni, S.; Bonini, N.; Calandra, M.; Car, R.; Cavazzoni, C.; Ceresoli, D.; Chiarotti, G. L.; Cococcioni, M.; Dabo, I.; Dal Corso, A.; de Gironcoli, S.; Fabris, S.; Fratesi, G.; Gebauer, R.; Gerstmann, U.; Gougoussis, C.; Kokalj, A.; Lazzeri, M.; Martin Samos, L.; Marzari, N.; Mauri, F.; Mazzarello, R.; Paolini, S.; Pasquarello, A.; Paulatto, L.; Sbraccia, C.; Scandolo, S.; Sclauzero, G.; Seitsonen, A. P.; Smogunov, A.; Umari, P.; Wentzcovitch, R. M. QUANTUM ESPRESSO: a modular and open source software project for quantum simulations of materials. *J. Phys.: Condens. Matter* **2009**, *21* (39), 395502.
(24) Giraudo, N.; Bergdolt, S.; Laye, F.; Krolla, P.; Lahann, J.; Thissen, P. Dehydration and dehydroxylation of C S H phases synthesized on silicon wafers. *Appl. Surf. Sci.* **2018**, *433*, 589−595.
(25) Giraudo, N.; Wohlgemuth, J.; Bergdolt, S.; Heinle, M.; Thissen, P. Passivation of Hydrated Cement. *ACS Sustainable Chem. Eng.* **2018**, *6* (1), 727−737.
(26) Monkhorst, H. J.; Pack, J. D. Special points for Brillouin zone integrations. *Phys. Rev. B* **1976**, *13* (12), 5188−5192.
(27) Perdew, J. P.; Burke, K.; Ernzerhof, M. Generalized Gradient Approximation Made Simple. *Phys. Rev. Lett.* **1996**, *77* (18), 3865−3868.
(28) Amato, I. Green cement: Concrete solutions. *Nature* **2013**, *494*, 300−301.
(29) Nishi, F. Strontium Metasilicate, $SrSiO_3$. *Acta Crystallogr., Sect. C: Cryst. Struct. Commun.* **1997**, *53* (5), 534−536.
(30) Scherrer, P. Bestimmung der Größe und der inneren Struktur von Kolloidteilchen mittels Röntgenstrahlen. *Math. Phys.* **1918**, *2*, 98−100.
(31) Almasri, K. A.; Sidek, H. A. A.; Matori, K. A.; Zaid, M. H. M. Effect of sintering temperature on physical, structural and optical properties of wollastonite based glass ceramic derived from waste soda lime silica glasses. *Results Phys.* **2017**, *7*, 2242−2247.
(32) Nishi, F.; Takéuchi, Y. The rhombohedral structure of tricalcium silicate at 1200 C. *Zeitschrift für Kristallographie Crystalline Materials* **1984**, *168* (1−4), 197−212.
(33) Takeuchi, Y.; Nishi, F.; Maki, I. Structural Aspects Of The Phase Transitions In Tricalcium Silicate Ca_3SiO_5 (C_3S). *Acta Crystallogr., Sect. A*, **1984**, C215−C216.
(34) Liu, S. S.; Li, H.; Xiao, W. D. Sintering effect on crystallite size, hydrogen bond structure and morphology of the silane derived silicon powders. *Powder Technol.* **2015**, *273*, 40−46.
(35) Brus, L. Electronic wave functions in semiconductor clusters: experiment and theory. *J. Phys. Chem.* **1986**, *90* (12), 2555−2560.
(36) Brus, L. E. Electron electron and electron hole interactions in small semiconductor crystallites: The size dependence of the lowest excited electronic state. *J. Chem. Phys.* **1984**, *80* (9), 4403−4409.
(37) Longo, R. C.; Cho, K.; Hohmann, S.; Thissen, P. Mechanism of Phosphorus Transport Through Silicon Oxide During Phosphonic Acid Monolayer Doping. *J. Phys. Chem. C* **2018**, *122* (18), 10088−10095.
(38) Longo, R. C.; Cho, K.; Brüner, P.; Welle, A.; Gerdes, A.; Thissen, P. Carbonation of Wollastonite(001) Competing Hydration: Micro scopic Insights from Ion Spectroscopy and Density Functional Theory. *ACS Appl. Mater. Interfaces* **2015**, *7* (8), 4706−4712.
(39) Chevrier, V. L.; Ong, S. P.; Armiento, R.; Chan, M. K. Y.; Ceder, G. Hybrid density functional calculations of redox potentials and formation energies of transition metal compounds. *Phys. Rev. B: Condens. Matter Mater. Phys.* **2010**, *82* (7), 075122.
(40) Schönberger, U.; Aryasetiawan, F. Bulk and surface electronic structures of MgO. *Phys. Rev. B: Condens. Matter Mater. Phys.* **1995**, *52* (12), 8788−8793.
(41) Nils, W.; Arnold, F. H.; Nils, W.; Egon, W.; Gerd, F. *Lehrbuch der Anorganischen Chemie*; De Gruyter: Berlin, 2008.
(42) Schwetlick, K. *Organikum: organisch chemisches Grundpraktikum*; Wiley VCH: 2015.
(43) Efimov, A. M. *Optical Constants of Inorganic Glasses*; Taylor & Francis: 1995.

(44) Tian, R.; Seitz, O.; Li, M.; Hu, W.; Chabal, Y. J.; Gao, J. Infrared Characterization of Interfacial Si O Bond Formation on Silanized Flat SiO_2/Si Surfaces. *Langmuir* **2010**, *26* (7), 4563−4566.
(45) Lisovskii, I. P.; Litovchenko, V. G.; Lozinskii, V. G.; Steblovskii, G. I. IR spectroscopic investigation of SiO_2 film structure. *Thin Solid Films* **1992**, *213* (2), 164−169.
(46) Burger, S.; Ehrenreich, M. G.; Kieslich, G. Tolerance factors of hybrid organic inorganic perovskites: recent improvements and current state of research. *J. Mater. Chem. A* **2018**, *6* (44), 21785−21793.
(47) Longo, R. C.; Mattson, E. C.; Vega, A.; Cabrera, W.; Cho, K.; Chabal, Y. J.; Thissen, P. Mechanism of Arsenic Monolayer Doping of Oxide Free Si(111). *Chem. Mater.* **2016**, *28* (7), 1975−1979.
(48) Mohammadi Hafshejani, T.; Hohmann, S.; Nefedov, A.; Schwotzer, M.; Brenner Weiss, G.; Izadifar, M.; Thissen, P. Formation and Stability of Nontoxic Perovskite Precursor. *Langmuir* **2019**, *35* (49), 16217−16225.
(49) Ebbert, C.; Grundmeier, G.; Buitkamp, N.; Kröger, A.; Messerschmidt, F.; Thissen, P. Toward a microscopic understanding of the calcium silicate hydrates/water interface. *Appl. Surf. Sci.* **2014**, *290*, 207−214.
(50) Kang, F.; Sun, G.; Boutinaud, P.; Wu, H.; Ma, F. X.; Lu, J.; Gan, J.; Bian, H.; Gao, F.; Xiao, S. Recent advances and prospects of persistent luminescent materials as inner secondary self luminous light source for photocatalytic applications. *Chem. Eng. J.* **2021**, *403*, 126099.
(51) Burek, K.; Krause, F.; Schwotzer, M.; Nefedov, A.; Süssmuth, J.; Haubitz, T.; Kumke, M. U.; Thissen, P. Hydrophobic Properties of Calcium Silicate Hydrates Doped with Rare Earth Elements. *ACS Sustainable Chem. Eng.* **2018**, *6* (11), 14669−14678.